

# Quantifying Losses and Assessing the Photovoltage Limits in Metal–Insulator–Semiconductor Water Splitting Systems

John Hemmerling, Joseph Quinn, and Suljo Linic\*

Metal–insulator–semiconductor (MIS) photo-electrocatalysts offer a pathway to stable and efficient solar water splitting. Initially motivated as a strategy to protect the underlying semiconductor photoabsorber from harsh operating conditions, the thickness of the insulator layer in MIS systems has recently been shown to be a critical design parameter which can be tuned to optimize the photovoltage. This study analyzes the underlying mechanism by which the thickness of the insulator layer impacts the performance of MIS photo-electrocatalysts. A concrete example of an Ir/HfO<sub>2</sub>/n-Si MIS system is investigated for the oxygen evolution reaction. The results of combined experiments and modeling suggest that the insulator thickness affects the photovoltage i) favorably by controlling the flux of charge carriers from the semiconductor to the metal electrocatalyst and ii) adversely by introducing nonidealities such as surface defect states which limit the generated photovoltage. It is important to quantify these different mechanisms and suggest avenues for addressing these nonidealities to enable the rational design of MIS systems that can approach the fundamental photovoltage limits. The analysis described in this contribution as well as the strategy toward optimizing the photovoltage are generalizable to other MIS systems.

## 1. Introduction


Harnessing sunlight to split water is a sustainable route to produce hydrogen fuel. A promising system for photo-electrochemical water splitting consists of two semiconductor light absorbers each coupled to an electrocatalyst. These tandem systems can achieve higher efficiencies than single semiconductor systems since they absorb a larger fraction of the solar spectrum while generating sufficient photovoltage to split water. An efficiency analysis of these dual semiconductor systems has demonstrated that the optimal bandgap is  $\approx 1\text{--}1.4$  eV for the bottom absorber and  $\approx 1.7\text{--}2.1$  eV for the top absorber.<sup>[1–3]</sup> Among semiconductors that exhibit an adequate bandgap, silicon (bandgap of 1.1 eV) has emerged as a promising choice due to its earth-abundance and wide-spread use in the electronics

and solar cell industry.<sup>[4–8]</sup> A common strategy to obtain high photovoltage with Si has been to fabricate traditional p–n Si homojunctions.<sup>[9–13]</sup> Furthermore, significant effort has been focused on improving catalytic activity<sup>[14–18]</sup> of electrocatalysts attached to Si and increasing solar utilization by nanostructuring Si and/or introducing plasmonic materials.<sup>[19–23]</sup> Besides improving efficiency, another critical challenge with Si and almost all other semiconductors with the desired bandgap ( $\approx 1\text{--}2.1$  eV) is their chemical instability in the electrolyte under photocatalytic water oxidation conditions.<sup>[24–27]</sup>

In recent years, it has been demonstrated that oxide insulator materials can be used to protect and stabilize the low bandgap semiconductors in metal–insulator–semiconductor (MIS) device architectures. Many insulators have been utilized in silicon-based MIS photocatalyst systems. These include SiO<sub>2</sub>,<sup>[28–41]</sup> TiO<sub>2</sub>,<sup>[42–47]</sup> HfO<sub>2</sub>,<sup>[48,49]</sup> Al<sub>2</sub>O<sub>3</sub>,<sup>[42,50–53]</sup> SrTiO<sub>3</sub>,<sup>[54]</sup> and

ZrO<sub>2</sub>.<sup>[55]</sup> Initially, MIS systems were motivated by their ability to improve the chemical stability of semiconductors, but recently many design strategies have been identified to improve the efficiency of these systems. In general, a large barrier height, low resistance, and ideal interfaces with minimal defects are necessary to achieve high efficiencies and photovoltages in MIS systems. One design strategy to generate a large barrier height and photovoltage in MIS systems is to use high work function metals for n-type systems (low work function metals for p-type systems).<sup>[49,52,56]</sup> Another strategy to obtain a large barrier height is through the pinch-off effect, where a high barrier electrolyte or oxide can compensate for low barrier electrocatalytic metal nanoparticles.<sup>[29,32,34,40,41,57]</sup> Previous reports have also demonstrated that the insulator layer can serve as a passivation layer to remove defects and minimize barrier height losses from Fermi level pinning.<sup>[50,51,53]</sup> Furthermore, several studies have shown that annealing is an effective method to further passivate interfacial defects and improve the photovoltage.<sup>[31,45,47]</sup> Recently, it has been demonstrated that the thickness of the insulator is a critical design parameter which can be tuned to maximize the photovoltage.<sup>[48,49,52]</sup> For example, we have shown that the thickness of the HfO<sub>2</sub> tunnel insulator significantly impacts the photovoltage generated by Ni/HfO<sub>2</sub>/n-Si MIS system in photo-electrocatalytic water oxidation.<sup>[48]</sup> We demonstrated that by tuning the thickness of the HfO<sub>2</sub> insulator we can tune the flux of minority and majority charge carriers from

J. R. Hemmerling, Dr. J. P. Quinn, Prof. S. Linic  
Department of Chemical Engineering  
Catalysis Science and Technology Institute  
University of Michigan  
2800 Plymouth Road, Ann Arbor, MI 48109, USA  
E-mail: linic@umich.edu

 The ORCID identification number(s) for the author(s) of this article can be found under <https://doi.org/10.1002/aenm.201903354>.

DOI: 10.1002/aenm.201903354

the semiconductor to the electrocatalyst and therefore minimize the rate of charge recombination and maximize the photovoltage. While significant performance improvements have been achieved in MIS systems, the key performance-limiting parameters are often not evaluated, and the theoretical photovoltage maximum is typically not quantified. Therefore, it is generally unclear how close a system is to approaching its optimal performance or what specific parameters are limiting the performance.

In this contribution, we analyze and quantify the underlying mechanisms by which the thickness of an insulator impacts the photovoltage of the MIS photo-electrocatalysts. We performed our studies by focusing on a concrete example of a model Ir/HfO<sub>2</sub>/n-Si MIS system for the oxygen evolution reaction (OER). Additionally, we use MIS diode theory to design experiments and quantify key metrics to assess the overall performance and photovoltage limits. We find that while the insulator thickness controls the flux of charge carriers from the semiconductor to the electrocatalysts (and therefore controls the charge recombination), which can be very beneficial, the introduction of additional interfaces in the system can simultaneously decrease the inherent semiconductor/electrocatalysts barrier height. These losses are manifested in large and unfavorable ideality factors. We demonstrate that surface defects states are the likely source of these nonidealities and suggest avenues for improving the ideality factor and achieving photovoltages close to the fundamental limit. The strategies and underlying physics described in this work are general to other MIS systems and provide insights to further optimize the photovoltage in MIS systems for water splitting applications.

## 2. Results and Discussion

### 2.1. MIS System Fabrication and Characterization

The MIS systems consisted of n-type silicon (n-Si) or degenerately doped p<sup>+</sup>-Si covered by HfO<sub>2</sub> that was deposited using atomic layer deposition (ALD). The thickness of the insulator HfO<sub>2</sub> layer was controlled by varying the number of ALD cycles from 0 to 25 resulting in 0–3 nm thick HfO<sub>2</sub>. ALD is a widely used method to deposit pinhole-free, uniform layers with sub-nanometer precision.<sup>[56,58]</sup> Evidence for absence of pinholes is provided in Figure S3 (Supporting Information). After the HfO<sub>2</sub> deposition, a 3.5 nm Ir layer was deposited by direct current magnetron sputtering. Further details of the fabrication are provided in the Experimental Section.

To characterize the MIS samples, we performed scanning transmission electron microscopy (STEM) on cross sections of the Ir/HfO<sub>2</sub>/n-Si samples as shown in Figure 1 (additional STEM cross-sectional images are shown in Figures S1 and S2, Supporting Information). The cross-sectional images show clearly identifiable components of the layered nanostructures

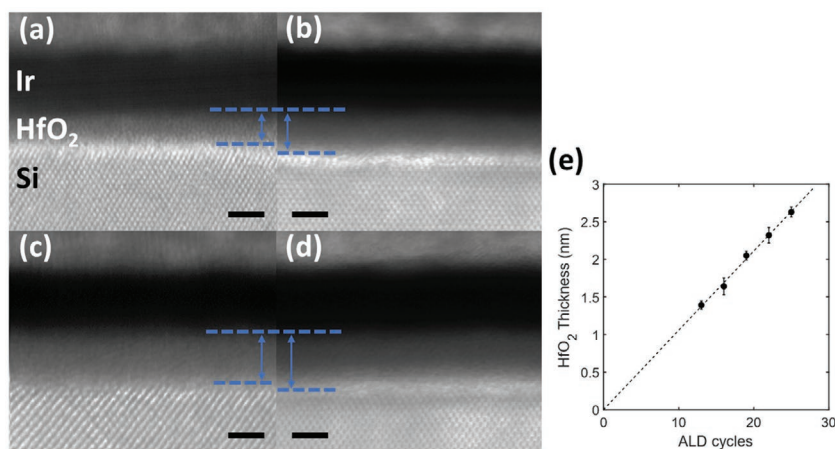


**Figure 1.** Characterization of 3.5 nm-Ir/x-HfO<sub>2</sub>/n-Si. Cross-sectional STEM images for a) 16 cycles (1.6 nm) HfO<sub>2</sub>, b) 19 cycles (2.0 nm) HfO<sub>2</sub>, c) 22 cycles (2.3 nm) HfO<sub>2</sub>, and d) 25 cycles (2.6 nm) HfO<sub>2</sub>. The blue dashed lines mark the boundaries between the HfO<sub>2</sub> and the metal and semiconductor. The blue arrows represent the thickness of the HfO<sub>2</sub> layer. The black scale bars are 2 nm. e) HfO<sub>2</sub> thicknesses as a function of the number of HfO<sub>2</sub> ALD cycles.

and defined boundaries between the different components. Data in Figure 1e shows the HfO<sub>2</sub> thickness as a function of the ALD cycles used in the fabrication process. On average one ALD cycle results in ≈0.1 nm of deposited HfO<sub>2</sub>. While the native SiO<sub>2</sub> layer on Si was etched away prior to HfO<sub>2</sub> deposition, an adventitious SiO<sub>2</sub> layer may form during ≈5 min exposure to atmosphere or during exposure to water at high temperatures in the ALD reactor. The SiO<sub>2</sub> layer is evident from the ≈0.5 nm white layer between the Si and HfO<sub>2</sub>. An adventitious SiO<sub>2</sub> layer has been observed in other ALD studies on HF-etched Si,<sup>[31,48,53]</sup> and it was similar for all samples so its effect should be uniform among samples.

### 2.2. Photovoltage Measurements

To evaluate the performance of these MIS materials in photocatalytic OER, we performed cyclic voltammetry (CV) measurements and linear sweep voltammetry (LSV) in a three-electrode setup under 1 sun illumination in an oxygen-saturated 1 M KOH electrolyte (Figure 2a). Additional CV measurements were performed in 1 M KCl and 10/10 × 10<sup>−3</sup> M Ferri/Ferrocyanide (FFC), measuring the reduction and oxidation of the FFC redox couple (Figure 2b). For OER experiments in KOH experiments, the photovoltage is defined as the difference between the voltage at a current of 1 mA cm<sup>−2</sup> for the illuminated n-Si samples and the voltage at a current of 1 mA cm<sup>−2</sup> for the dark p<sup>+</sup>-Si control system. For FFC experiments, the photovoltage is defined as the difference between the open-circuit voltage (the voltage when the net current is 0 mA cm<sup>−2</sup>) of the n-Si and p<sup>+</sup>-Si samples. As shown in Figure 2c, the photovoltages measured in KOH and FFC are similar for each MIS system. The data show that the photovoltage improves considerably as the HfO<sub>2</sub> thickness increases from 0–2.0 nm HfO<sub>2</sub> (0–19 ALD cycles), plateaus between 2.0–2.3 nm (19–22 cycles), and decreases for greater thickness. Specifically, the photovoltage increases by 160 mV, from 330 mV for 0 nm HfO<sub>2</sub> to 480 mV for 2.0 nm HfO<sub>2</sub>.

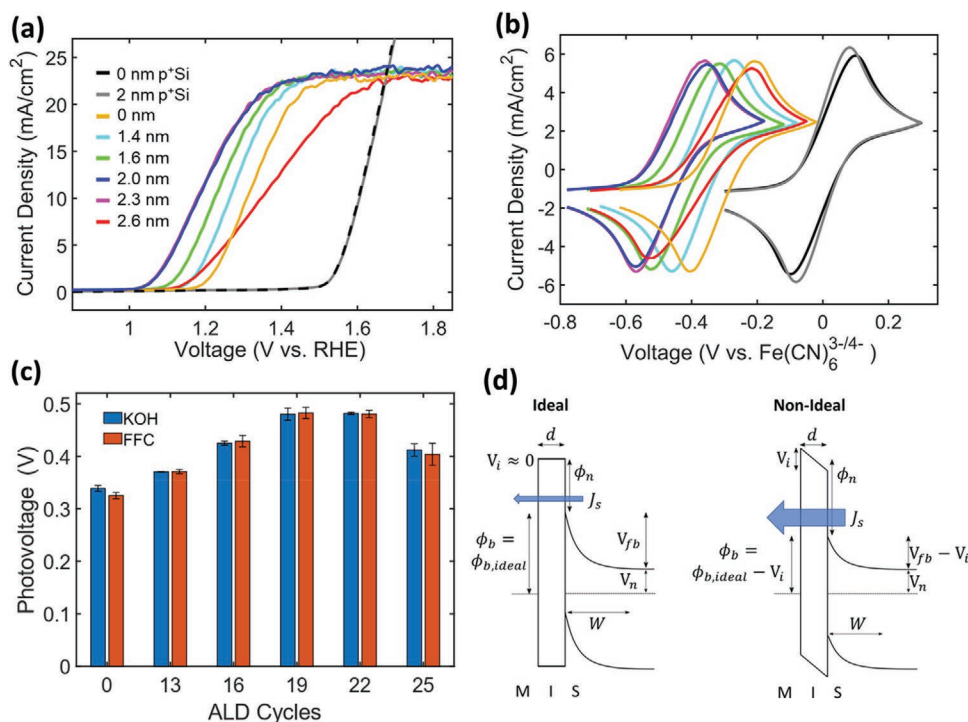


**Figure 2.** Electrochemical testing of the 3.5 nm-Ir/x-HfO<sub>2</sub>/n-Si and 3.5 nm-Ir/x-HfO<sub>2</sub>/p<sup>+</sup>-Si samples. a) LSV curves upon 1 sun illumination in 1 M KOH. b) CVs upon 1 sun illumination in 10/10 × 10<sup>-3</sup> M FFC and 1 M KCl. The legend in a) also corresponds to the curves in b). c) Photovoltage measured at 1 mA cm<sup>-2</sup> in KOH and measured at open-circuit potential in FFC. d) Energy band diagrams in dark at equilibrium (zero bias, V<sub>a</sub> = 0) for an ideal (n = 1) and a nonideal (n > 1) MIS system. The ideal system has no voltage drop in the insulator, so its barrier height is equivalent to the ideal value (φ<sub>b</sub> = φ<sub>b,ideal</sub>). The nonideal system has a significant insulator voltage drop, which lowers the barrier height relative to the ideal value (φ<sub>b</sub> = φ<sub>b,ideal</sub> - V<sub>i</sub>). The lower barrier height means a larger quantity of electrons can recombine in the metal, which is represented by the thicker blue arrow for the reverse saturation recombination current (J<sub>s</sub>). For the same insulator thickness, the nonideal sample will have the lower photovoltage due to this larger degree of recombination. The dotted lines are the equilibrated Fermi levels of the metal and semiconductor (i.e., the Si Fermi level is pinned to the metal during equilibration). Other variables in the figure are described in the main text.

The photovoltage loss for the thickest 2.6 nm HfO<sub>2</sub> sample is due to an additional resistance to charge transfer attributed to the thicker insulator layer, i.e., the resistance to tunneling through the insulator becomes large enough to limit the charge transfer rate. The resistance is evident by the lower slope and fill factor in Figure 2a and by the wider peak to peak splitting in Figure 2b. For 0–2.3 nm HfO<sub>2</sub> samples, the slopes and peak to peak splitting are similar, which indicates that these samples are in a thickness regime where the tunneling resistance is not the dominant loss in these systems. We also note that the performance of p<sup>+</sup>-Si with 0 and 2.0 nm HfO<sub>2</sub> are nearly identical, which further suggests that a thin HfO<sub>2</sub> layer does not significantly affect the series resistance.

The stability of a 3.5 nm-Ir/2.3 nm-HfO<sub>2</sub>/n-Si sample was analyzed in 1 M KOH using chronoamperometry while holding at 1.8 V versus RHE under 1 sun illumination. As shown in Figure S4a (Supporting Information) the current was stable for over 6 h with no signs of permanent degradation. CVs taken every 2 h are shown in Figure S4b (Supporting Information). The photovoltage and fill factor remained the same throughout the experiment which demonstrates the stability of these MIS systems.

### 2.3. MIS Tunnel Diode Theory

To explain the photovoltage enhancement as a function of the insulator thickness, we employed MIS tunnel diode theory to

analyze the flux of charge carriers from the semiconductor to the metal electrocatalyst. The generated photovoltage in these systems is determined by the net electron and net hole currents being transported to the metal catalyst which ultimately governs the electron/hole recombination. To optimize the photovoltage, the hole minority current reaching the metal electrocatalyst, performing the oxidation reaction, should be maximized. Similarly, the electron majority current reaching the metal, resulting in recombination, should be minimized. For a forward applied bias (−V<sub>a</sub> > 0), the net current (electrons plus holes) entering the metal electrocatalyst through the MIS junction (J<sub>MIS</sub>) is described by the illuminated diode equation

$$J_{\text{MIS}} = J_{\text{ph}} - J_s \exp\left(-\frac{qV_a}{nkT}\right) \quad (1)$$

J<sub>ph</sub> is the photocurrent density representing the quantity of holes generated upon illumination that migrate to the metal electrocatalyst, J<sub>s</sub> is the reverse saturation current density, q is the elementary charge, V<sub>a</sub> is the applied voltage, n is the ideality factor (n = 1 is ideal, n > 1 is nonideal), k is the Boltzmann constant, and T is temperature. The first and second term on the right side of Equation (1) represents the hole and electron currents, respectively. J<sub>s</sub> governs the electron recombination current, and it is desired to decrease J<sub>s</sub> as much as possible.

It is well known that the dominant recombination current in an MIS tunnel diode is due to thermionic emission corrected for tunneling<sup>[59]</sup>

$$J_s = A^* T^2 \exp\left(-\frac{q\phi_b(n)}{kT}\right) \exp(-\infty d\sqrt{\phi_n}) \quad (2)$$

Here,  $A^*$  represents the Richardson's constant,  $\phi_b(n)$  is the barrier height measured at equilibrium in dark (zero bias,  $V_a = 0$ ) and it is a function of the ideality factor ( $n$ ),  $\infty$  is a constant with units of  $\text{eV}^{-1/2} \text{Å}^{-1}$  to make the exponent dimensionless,  $d$  is the insulator thickness, and  $\phi_n$  is the mean insulator barrier for electrons defined by the difference between the insulator conduction band and semiconductor conduction band (see Figure 2d for representations of these variables). The term  $\exp(-\infty d\sqrt{\phi_n})$  accounts for the probability of electrons tunneling through a rectangular insulator barrier. In the limit of  $d$  approaching zero, the tunnel probability term goes to 1 and Equation (2) simplifies to the reverse saturation current of a metal–semiconductor Schottky diode. A larger  $d$  and  $\phi_n$  introduces a tunneling barrier which exponentially decreases electron recombination and improves photovoltage (as long as the insulator is not so thick that the tunneling resistance dominates the performance). This simple analysis qualitatively explains the improved photovoltage as a function of  $\text{HfO}_2$  thickness observed in Figure 2c.

Equation (2) suggests that increasing the barrier height ( $\phi_b$ ) is also important because it exponentially decreases the recombination term  $J_s$ . We note that  $\phi_b$  represents the potential barrier the electrons must overcome to recombine with holes in the metal, and it is defined as the difference between the metal Fermi level (work function) and the semiconductor conduction band edge, as illustrated in Figure 2d. In an ideal system, the insulator does not influence the barrier height, so the barrier height can be determined from the metal Fermi level and the semiconductor conduction band before contact or equilibration ( $\phi_b = \phi_{b,\text{ideal}}$ ). In experimental systems with nonidealities, the barrier height is lowered according to the following relationship<sup>[60]</sup>

$$\phi_b = \frac{\phi_{b,\text{ideal}}}{n} + \left(\frac{n-1}{n}\right)V_n \quad (3)$$

Here,  $V_n$  is the difference in energy between the Fermi level and conduction band in the bulk of the semiconductor, as illustrated in Figure 2d. In the limit as  $n = 1$ ,  $\phi_b$  equals its ideal value of  $\phi_{b,\text{ideal}}$ . When nonidealities are present in the system ( $n > 1$ ), the position of the semiconductor conduction band edge lowers relative to the metal Fermi level, so  $\phi_b$  is less than  $\phi_{b,\text{ideal}}$  (Figure 2d).

By plugging Equation (2) into Equation (1) and setting the net current ( $J_{\text{MIS}}$ ) to zero, the open-circuit photovoltage ( $V_{\text{oc}}$ ) for an MIS system is obtained

$$-V_{\text{oc}} \approx \frac{nkT}{q} \left[ \ln \frac{J_{\text{ph}}}{J_s} \right] = \frac{nkT}{q} \left[ \ln \frac{J_{\text{ph}}}{A^* T^2} + \frac{q}{kT} \phi_b(n) + \infty d\sqrt{\phi_n} \right] \quad (4a)$$

For the specific case of an ideal system ( $n = 1$ ), plugging Equation (3) into Equation (4a) yields the ideal open-circuit photovoltage ( $V_{\text{oc,ideal}}$ )

$$-V_{\text{oc,ideal}} = \frac{kT}{q} \left[ \ln \frac{J_{\text{ph}}}{A^* T^2} + \frac{q}{kT} \phi_{b,\text{ideal}} + \infty d\sqrt{\phi_n} \right] \quad (4b)$$

The open-circuit photovoltage is the photovoltage evaluated at equilibrium under illumination, and it is experimentally measured in Figure 2c. When nonidealities are present in the system ( $n > 1$ ), it is shown that  $|V_{\text{oc}}| < |V_{\text{oc,ideal}}|$  (see the Supporting Information for details). Therefore, any source of nonidealities will fundamentally limit the photovoltage and should be identified and avoided.

In MIS systems, a voltage drop in the insulator layer ( $V_i$  in Figure 2d) can be considered the dominant source of nonidealities (see the Supporting Information for justification). A high ideality factor corresponds to a large voltage drop in the insulator. As shown in Figure 2d, a large  $V_i$  results in a lower  $\phi_b$  relative to  $\phi_{b,\text{ideal}}$  (i.e.,  $\phi_b = \phi_{b,\text{ideal}} - V_i$ ). The insulator voltage drop is governed by Gauss's Law, where the combined charge from the semiconductor space charge (band bending) region and the interface defect states cause the insulator voltage drop. Assuming that the surface states are in equilibrium with the semiconductor, then an expression for the ideality factor, as previously derived, is<sup>[59]</sup>

$$n = 1 + \frac{d}{\epsilon_i} \left( \frac{\epsilon_s}{W} + qD_s \right) \quad (5)$$

Here,  $D_s$  is the density of surface states in equilibrium with the semiconductor,  $W$  is the width of the space charge region (illustrated in Figure 2d), and  $\epsilon_s$  and  $\epsilon_i$  are the semiconductor and insulator permittivity (see the Supporting Information for more details about this equation). The first term in the parentheses of Equation (5) is related to the charge in the space charge region which is a fundamentally unavoidable part of these systems. We note that this unavoidable voltage drop is less than 1 mV for the Ir/x- $\text{HfO}_2$ /n-Si MIS systems (see the Supporting Information for more details). The second term in parentheses is related to the density of the surface states, which are common in MIS systems but can be minimized by introducing high-quality interfaces. If other variables are nearly constant, then the ideality factor is expected to linearly increase with increasing insulator thickness ( $d$ ).

The above analysis demonstrates an inherent tradeoff of the insulator layer. The insulator layer improves the photovoltage by introducing an additional electron tunnel barrier which reduces recombination (Equations (2) and (4)), but it may also increase the ideality factor which lowers the barrier height (Equation (3)). The balance of these two factors ultimately determines to what extent the photovoltage can be optimized.

## 2.4. Experiments to Evaluate Ideality Factor and Recombination Current

To fully characterize the performance limits of the MIS systems, the variables in Equation (4), namely the ideality factor, the barrier height, and the tunneling probability term must be determined. To calculate the ideality factor for each  $\text{HfO}_2$  thickness, the open-circuit voltage was measured at



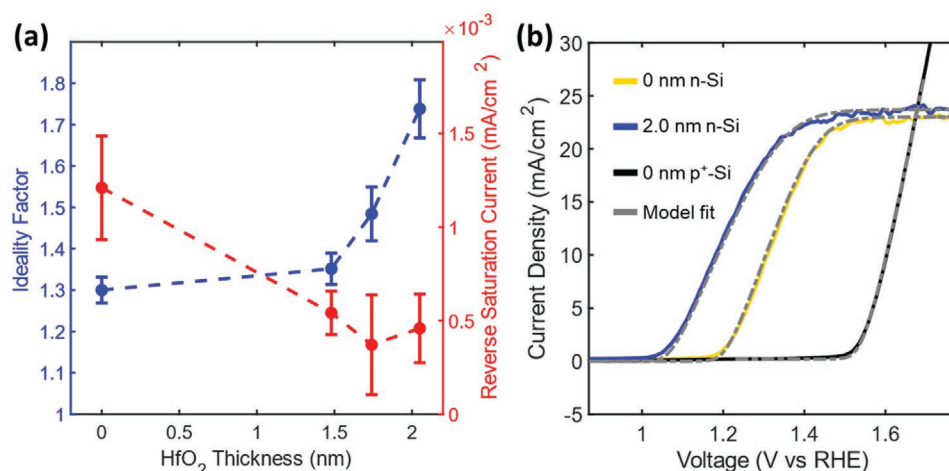


**Figure 3.** a) Ideality factor and reverse saturation current for 3.5 nm-Ir/*x*-HfO<sub>2</sub>/n-Si samples measured in 350/50 × 10<sup>-3</sup> M FFC and 1 M KCl. b) Comparison of experimental and modeled LSVs calculated for the 0 nm HfO<sub>2</sub> n-Si, 2.0 nm HfO<sub>2</sub> n-Si, and 0 nm HfO<sub>2</sub> p<sup>+</sup>-Si samples.

different light intensities.<sup>[29]</sup> From Equation (4), a plot of  $V_{oc}$  versus  $\ln(J_{ph})$  will yield a straight line. The slope of this line gives the ideality factor ( $n$ ) and the intercept gives the reverse saturation recombination current ( $J_s$ ).  $J_s$  and  $n$  are plotted in **Figure 3a** for the 0–2.0 nm HfO<sub>2</sub> samples. The 2.3 and 2.6 nm HfO<sub>2</sub> samples are in the thickness regime where the hole minority tunneling current is limited, so they cannot be accurately represented by Equation (1) and are not included in Figure 3a (see the Supporting Information for the thicker sample data and explanation). Figure 3b shows a comparison of experimental and modeled CVs for representative Ir/0 nm-HfO<sub>2</sub>/n-Si, Ir/2.0 nm-HfO<sub>2</sub>/n-Si, and Ir/0 nm-HfO<sub>2</sub>/p<sup>+</sup>-Si samples. The modeled CV data was obtained by plugging the measured  $n$  and  $J_s$  into Equation (1), and then coupling this MIS diode current to the Butler–Volmer equation which models the catalytic activity of the Ir (see the Supporting Information for details). The experiments agree very well with the model, which indicates that the ideality factor and reverse saturation current, which are measured in FFC, nicely capture the performance for these MIS systems under more complex OER conditions in KOH.

As shown in Figure 3a, the increase in the ideality factor is greater than linear, indicating that the density of surface states may be increasing with insulator thickness (Equation (5)). The calculation for density of surface states as a function of HfO<sub>2</sub> thickness are shown in Figure S7 (Supporting Information). The relationship between the impact of the surface states and the insulator thickness is consistent with previous reports<sup>[59]</sup> (see the Supporting Information). We note that the 0 nm HfO<sub>2</sub> sample exhibited a relatively high ideality factor of 1.3 even without the presence of an HfO<sub>2</sub> layer. Here, the nonidealities may be attributed to an interfacial SiO<sub>2</sub> layer, which has been widely discussed in the metal–semiconductor Schottky diode literature.<sup>[61]</sup> As previously discussed, the high ideality factor for each sample results in significant losses that limit the photovoltage. To quantify the extent of these photovoltage losses, first  $\phi_{b,ideal}$  and  $\phi_b$  must be determined.

## 2.5. Electrochemical Impedance Spectroscopy (EIS) Experiments

To calculate the ideal barrier height for each HfO<sub>2</sub> thickness, we used electrochemical impedance spectroscopy to measure the capacitance of the semiconductor space charge (band bending) region as the function of applied voltage. The impedance measurements were performed at a high enough frequency so that the surface states cannot generate significant capacitance or influence the calculated barrier height, i.e., at these frequencies the surface states are not charged or discharged<sup>[62]</sup> (see the Supporting Information for additional details). Therefore, the barrier height measured using this approach is the ideal barrier height, which would exist in the absence of surface states. The capacitance of the space charge region ( $C_{sc}$ ) in the semiconductor is given by the Mott–Schottky equation

$$\left(\frac{1}{C_{sc}}\right)^2 = \frac{2}{\epsilon_s A^2 q N_D} \left(V_a - V_{fb} - \frac{kT}{q}\right) \quad (6)$$

Here,  $A$  is the surface area,  $N_D$  is the doping density of the semiconductor,  $V_a$  is the applied voltage, and  $V_{fb}$  is the flat-band potential.  $V_{fb}$  is ideally defined by the difference between the Fermi levels of the semiconductor and the metal before contact or equilibration (see Equation (S16) in the Supporting Information). Furthermore,  $V_{fb}$  is the upper limit to the photovoltage that a system can generate in the limit of zero recombination. The ideal barrier height ( $\phi_{b,ideal}$ ) can be calculated from the flat-band potential

$$\phi_{b,ideal} = V_{fb} + V_n = V_{fb} + \frac{kT}{q} \ln\left(\frac{N_C}{N_D}\right) \quad (7)$$

Here,  $V_n$  is defined by the semiconductor doping density ( $N_D$ ) and the effective density of states in the semiconductor conduction band ( $N_C$ ). A Mott–Schottky plot is obtained by plotting  $1/C_{sc}^2$  against  $V_a$  as shown in **Figure 4a**. The slope of the line gives the n-Si doping density and the  $x$ -intercept gives the flat-band potential. The extracted values for  $\phi_{b,ideal}$ ,  $V_{fb}$ , and  $V_n$  as a function of HfO<sub>2</sub> thickness are shown in Figure 4b. All three

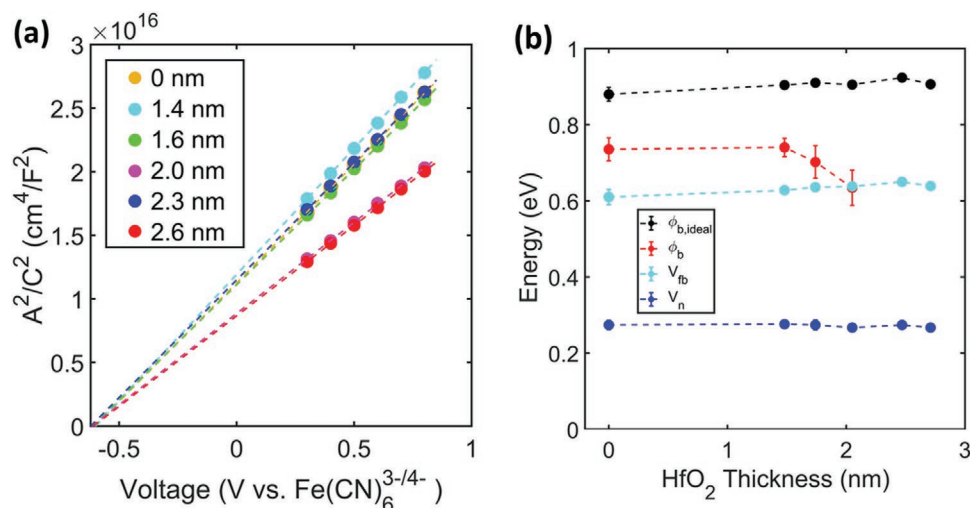


**Figure 4.** EIS and Mott-Schottky results for the 3.5 nm-Ir/x-HfO<sub>2</sub>/n-Si samples in  $10/10 \times 10^{-3}$  M FFC and 1 M KCl. a) Mott-Schottky plots in the dark showing the linear relationship and the extrapolated x-intercepts converged to a similar flat-band potential. b) Extracted values for the ideal flat-band barrier height, the barrier height, the flat-band potential, and  $V_n$  as a function of HfO<sub>2</sub> thickness. Values of  $\phi_b$  for the thicker HfO<sub>2</sub> samples are not provided because they are not accurately represented by Equations (1)–(4).

variables are largely independent of HfO<sub>2</sub> thickness. The measured ideal barrier height for each sample is  $\approx 0.9$  eV, which is similar to other Ir/n-Si Schottky diodes previously reported.<sup>[63]</sup> We also note that the doping densities calculated from the Mott-Schottky Equation (6) closely agree with four-point probe measurements (see Table S1, Supporting Information).

Now that  $\phi_{b,\text{ideal}}$  and  $n$  are known,  $\phi_b$  can be calculated using Equation (3) and the calculated values are shown in Figure 4b. The data show that the barrier height decreases with the insulator thickness due to the increasing ideality factor.

As previously discussed, this lowered barrier height likely manifests itself as a voltage drop in the insulator. The energy band diagrams in Figure 5 show the measured voltage drops in the insulator for the 1.4 nm HfO<sub>2</sub> and the 2.0 nm HfO<sub>2</sub> samples. For the 2.0 nm HfO<sub>2</sub> sample (Figure 5c), the barrier height drops to 0.63 eV due to a 0.27 eV voltage drop in the insulator layer ( $\phi_b = \phi_{b,\text{ideal}} - V_i$ ). This 0.63 eV barrier height is significantly lower than the 0.9 eV barrier for the ideal system in Figure 5a. Despite the lower barrier height, the 2.0 nm HfO<sub>2</sub> sample still yields the highest photovoltage (Figure 2c) because

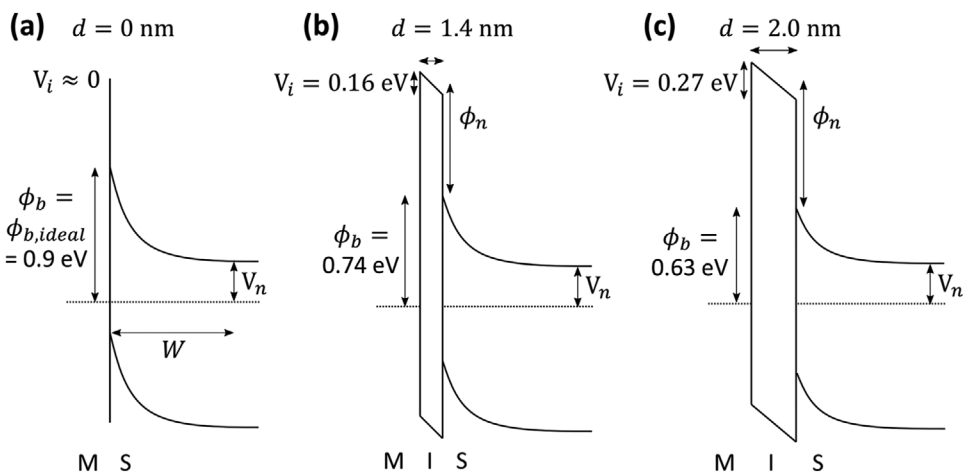


**Figure 5.** Energy band diagrams at equilibrium (zero bias,  $V_a = 0$ ) in the dark showing the effects of increasing the insulator thickness. a) Ideal metal-semiconductor system ( $n = 1$ ) with no insulator. For an ideal system,  $\phi_b = \phi_{b,\text{ideal}}$  (Equation (3)). b) MIS system with a thin insulator corresponding to the 1.4 nm HfO<sub>2</sub> sample. The nonideal insulator voltage drop results in a lower barrier height relative to the ideal system according to the relationship:  $\phi_b = \phi_{b,\text{ideal}} - V_i$ . c) MIS system with a thicker insulator corresponding to the 2.0 nm HfO<sub>2</sub> sample. The larger insulator voltage drop ( $V_i$ ) further lowers the barrier height relative to the ideal value. Despite the lower barrier height, the 2.0 nm sample in c) yields the highest photovoltage because the thick insulator significantly lowers the tunneling probability term which offsets the losses associated with the lower barrier height. The photovoltage of this system can be further improved by minimizing the insulator voltage drop. The barrier heights for each system are taken from Figure 4b. The insulator voltage drops in (b,c) correspond to the ideality factors in Figure 3a. The bandgap of the semiconductor in the diagrams is 1.11 eV with doping density ( $N_D$ ) corresponding to the Si used in this study. The dotted lines are the equilibrated Fermi levels of the metal and semiconductor.

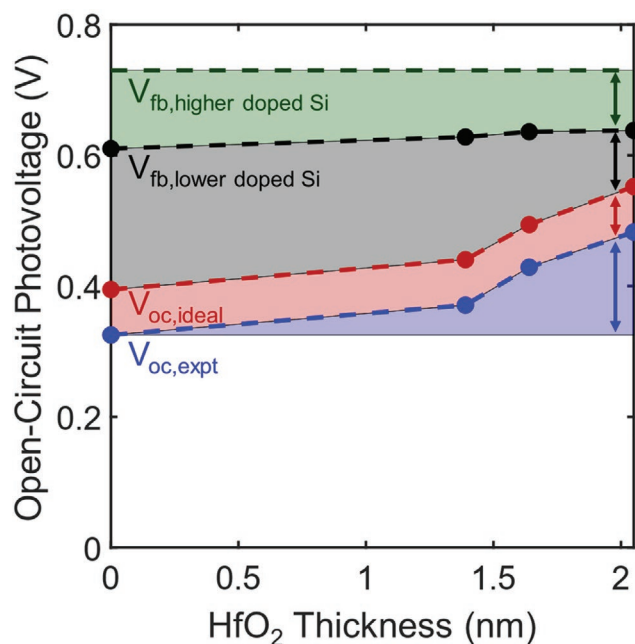


**Figure 6.** Experimental open-circuit photovoltages (blue points) taken from Figure 2 compared to the photovoltages for an ideal system (red points). The black data points are the flat-band potentials (i.e., maximum achievable photovoltage) for the lower doped n-Si samples ( $\approx 7 \times 10^{14} \text{ cm}^{-3}$ ) used in this study. The green dashed line represents the maximum photovoltage that can be achieved using higher doped n-Si ( $1.5 \times 10^{16} \text{ cm}^{-3}$ ). The blue region/arrow represents the 160 mV photovoltage improvement that can be obtained by tuning the insulator thickness. The red region/arrow represents the 70 mV photovoltage improvement that can be obtained by passivating surface states and creating ideal systems ( $n = 1$ ). The gray/black region/arrow represents the 80 mV losses associated with sub-optimal insulator characteristics and alternative recombination mechanisms. The green region/arrow represents improvements to the flat-band potential that can be obtained by increasing the doping density of the silicon.

the thicker insulator significantly lowers the tunneling probability term which offsets the losses associated with the lower barrier height. The tunneling probability term  $\exp(-\alpha d \sqrt{\chi})$  can be quantified using Equation (3) since  $J_s$  and  $\phi_b$  are known. The tunneling probability term as a function of insulator thickness is provided in Figure S12 (Supporting Information). As expected, increasing insulator thickness exponentially decreases the tunnel probability term as the electron charge transfer is impeded. For the 2.0 nm  $\text{HfO}_2$  sample, the tunnel probability term decreases the reverse saturation recombination current by a factor of nearly 500, which is the reason it achieves the highest photovoltage despite having the lowest barrier height.

## 2.6. Assessing Photovoltage Losses

Now that all the variables in Equation (4) have been experimentally measured, the open-circuit photovoltage of an ideal system can be compared to the experimental values. In this analysis, it is assumed that the tunneling probability term for a given  $\text{HfO}_2$  thickness is the same for ideal and nonideal systems. The blue region/arrow in Figure 6 represents the experimentally

observed 160 mV improvement to the photovoltage that is obtained by tuning the insulator thickness and exploiting the tunneling mechanisms to control the flux of excited charge carriers. The red region/arrow in Figure 6 demonstrates that ideal systems can achieve a  $\approx 70$  mV improvement in photovoltage compared to the experimental nonideal systems. This analysis suggests that nonidealities significantly lower the photovoltage for the present Ir/x- $\text{HfO}_2$ /n-Si MIS systems. Therefore, strategies to remove nonidealities, such as by annealing the samples to restructure the interfaces, are important to optimize the photovoltage. Previous work has demonstrated the utility of annealing  $\text{TiO}_2$  based MIS systems to improve photovoltage,<sup>[45,47]</sup> although the improvements were not quantified in the context of directly influencing the ideality factor and barrier height. As a proof of concept, we have performed a 30 min, 300 °C forming gas anneal on a sample with 2.0 nm of  $\text{HfO}_2$ , followed by depositing the Ir catalyst. The photovoltage increased to 510 mV, which is a 30 mV improvement compared to the nonannealed control sample (see Figure S13 in the Supporting Information). A 30 mV photovoltage increase is a significant improvement, but according to data in Figure 6, an additional 40 mV increase is possible from further optimization of the annealing procedure to remove the nonidealities.

We also emphasize the importance of the flat-band potential, which represents the maximum photovoltage that can be extracted from the system in the limit of zero recombination. With an optimal insulator thickness and an ideal system, the achievable photovoltage is  $\approx 550$  mV, which is still 80 mV less than the  $\approx 630$  mV flat-band potential (black region/arrow in Figure 6). This 80 mV photovoltage loss is partially due to the relatively low barrier to tunneling for electrons ( $\phi_n$ ) provided by the  $\text{HfO}_2$  layer (see Figure S12 and corresponding discussion, Supporting Information). More specifically, the difference in the barrier to tunneling for holes and electrons in the case of  $\text{HfO}_2$  is not sufficient to maximize the performance of the system. These losses can be minimized by engineering a superior insulator layer with a larger barrier for electrons ( $\phi_n$ , decreasing reverse saturation recombination current), and a smaller barrier for holes ( $\phi_p$ , decreasing the tunneling resistance losses). We note that even with a perfect insulator, some losses below the flat-band potential will persist due to alternative recombination pathways such as bulk radiative recombination or back surface recombination.

Because the flat-band potential ultimately limits the maximum achievable photovoltage, strategies to further increase the flat-band potential are also critical. One method to improve the flat-band potential is to use higher work function metals (see Equation (S16) in the Supporting Information), which has been evaluated in previous reports.<sup>[49,52]</sup> Another way to achieve a higher flat-band potential is by using a higher doped Si substrate, although we note that there is a limit to which the doping can be increased before introducing additional recombination pathways from field emission and Auger recombination.<sup>[61]</sup> As a proof of concept, we have synthesized an Ir/19 cycle- $\text{HfO}_2$ /n-Si system with a higher doping of  $1.5 \times 10^{16} \text{ cm}^{-3}$  which corresponds to a  $V_n$  of 0.19 eV. The system achieved a flat-band potential of 0.73 V, and this limit has been included as the green dashed line in Figure 6. Despite the large flat-band potential, the system only achieved a photovoltage of 450 mV

due to an unfavorable ideality factor of 2.7 (see Figure S14 in the Supporting Information). The photovoltage for the higher doped Si sample is 280 mV below the flat-band potential, even for an optimal  $\approx 2.0$  nm  $\text{HfO}_2$  thickness. Therefore, the importance of minimizing losses from high ideality factors is particularly important for the higher doped n-Si MIS sample.

Finally, we note that several MIS water splitting systems have achieved over 600 mV of photovoltage through a combination of using relatively high doped Si and using high-quality oxides with minimal surface states.<sup>[30,45,53]</sup> As shown by the black region in Figure 6, even an ideal system with optimized insulator thickness may still fall significantly short of the photovoltage limits. The flat-band potential and the ideality factor are often not evaluated in previous studies, so it is unknown exactly how close these systems are to achieving their maximum theoretical photovoltage. Understanding how close a system is to achieving the performance limits is critical for the rational design of systems with even higher photovoltages. Furthermore, measuring the ideality factor is important to identify the source of the losses and overcome these limitations. The methods used in this paper can be applied to any MIS system to quantify the photovoltage limits and identify specific opportunities to improve efficiency.

### 3. Conclusion

We have found that a high ideality factor and corresponding decrease in the barrier height can significantly limit the photovoltage of MIS systems. While increasing the insulator thickness to 2.0 nm improves photovoltage by decreasing electron recombination through the tunnel probability term, there is a simultaneous lowering of the barrier height caused by nonidealities. For the case of Ir/ $\text{HfO}_2$ /n-Si MIS systems investigated here, the photovoltage can be improved by up to 70 mV by removing these nonidealities. Therefore, significant effort should be focused on achieving more ideal systems. Surface defect states are the most likely cause for the high ideality factor in the Ir/ $\text{HfO}_2$ /n-Si systems in this study. Passivating these defect states through annealing is a promising strategy to improve the ideality factor and the photovoltage. The results also show that even an ideal system with optimized insulator thickness may still fall significantly short of the maximum achievable photovoltage governed by the flat-band potential. To achieve the upper photovoltage limits, new insulators must be engineered with a larger barrier for electrons and a smaller barrier for holes (i.e., charge carrier selective insulators). The experiments outlined in the paper should be used in other MIS systems to determine the maximum obtainable photovoltage and to quantitatively assess what limits the efficiency for the specific system.

### 4. Experimental Section

**MIS Sample Fabrication:** Phosphorus doped (n-type, resistivity 1–10  $\Omega$  cm, (100)-oriented, 525  $\mu\text{m}$ ) Si wafers were purchased from Silicon Valley Microelectronics. Boron doped (p-type, resistivity 0.001–0.005, (100)-oriented, 525  $\mu\text{m}$ ) were purchased from Addison Engineering. Wafers were cleaned with NanoStrip (a commercial piranha

solution) for 10 min at 60  $^\circ\text{C}$  and dipped in buffered hydrofluoric acid for 1 min. Wafers were rinsed in water, spun dry, and then immediately placed in the ALD chamber. Thin (1–3 nm)  $\text{HfO}_2$  layers were deposited on whole wafers using a Veeco Fiji Atomic Layer Deposition System. In this process the ALD chamber is pumped down to 25 mT and preheated to 200  $^\circ\text{C}$ . The substrate is exposed to a number of ALD cycles in order to deposit a monolayer of  $\text{HfO}_2$ . An ALD cycle consists of a precursor dose of Tetrakis(dimethylamino)hafnium (TDMAH) for 250 ms followed by a 12 s purge and a 60 ms  $\text{H}_2\text{O}$  dose followed by a 12 s purge. The deposition occurred at a temperature of 200  $^\circ\text{C}$ . After the ALD process a 3–3.5 nm Ir layer was deposited on the  $\text{HfO}_2$ -coated wafers at a rate of  $1.1 \text{ \AA s}^{-1}$  using sputter deposition with a Lab 18-02 system. A DC power of 100 W was used and the working pressure was 4  $\mu\text{Torr}$ . Finally, the wafers were diced into  $13 \times 13$  mm squares using a dicing saw.

**MIS Sample Characterization:** Scanning transmission electron microscopy was performed with a JEOL 2100 probe-corrected analytical electron microscope with an accelerating voltage of 200 kV. The samples were prepared via focused ion-beam milling with a FEI Nova 200 nanolab SEM/FIB apparatus. Bright field STEM images were used to measure  $\text{HfO}_2$  thickness. The  $\text{HfO}_2$ /Ir boundary is marked by a change in contrast at the interfaces. The thicknesses were measured by analyzing cross-sectional images with IMAGEJ software at various points throughout the sample.

**Electrochemical Testing:** Electrochemical measurements were performed in a three-electrode cell. For all experiments, diced samples were housed in a 3D-printed electrode. The back contacts of the samples were scratched with a SiC scribe to remove the native oxide, and a gallium–indium eutectic was applied to ensure ohmic contact. The back contacts were then pressed against a copper plate. The working electrode's exposure to electrolyte was defined by an O-ring which also prevented the electrolyte from leaking to the back contact. The samples were exposed to a light source via a  $0.264 \text{ cm}^2$  aperture. Samples were illuminated using a 300 W UV 16S-Series Solar Simulator (Solar Light Company) with AM 1.5G filter. Light intensity was calibrated to  $100 \text{ mW cm}^{-2}$  with a photodiode.

A 1 M KOH (Fischer Scientific) electrolyte was used for the water oxidation measurements. n-type samples were illuminated by  $100 \text{ mW cm}^{-2}$  (1 sun) simulated light and p-type samples were measured in the dark. A graphite rod counter electrode and an Hg/HgO reference electrode were used in the three-electrode setup. Cyclic voltammetry and linear sweep voltammetry was performed with a scan rate of  $100 \text{ mV s}^{-1}$ . Oxygen was bubbled into the electrolyte throughout the experiments and the electrolyte was magnetically stirred. The following equation was used in order to convert from the Hg/HgO reference to the RHE at pH 14

$$V_{\text{RHE}} = V_{\text{Hg/HgO}} + 0.118 + 0.591 \cdot \text{pH} \quad (8)$$

A Ferri-/ferrocyanide solution consisting of  $10 \times 10^{-3} \text{ M}$  potassium hexacyanoferrate(II) trihydrate,  $10 \times 10^{-3} \text{ M}$  potassium hexacyanoferrate(III) (EMD Millipore), and 1 M KCl (Fischer Scientific) was used for measuring the open-circuit photovoltage and performing electrochemical impedance spectroscopy. The electrolyte was stagnant for the CV experiments, but was stirred for open-circuit voltage measurements and EIS experiments. A graphite reference electrode and Pt wire counter electrode were used such that the applied voltage is relative to the FFC redox potential. The samples were illuminated using the same conditions described above, and the CVs were performed with a scan rate of  $100 \text{ mV s}^{-1}$ . After each cycle, the open-circuit voltage was measured as the system reaches equilibrium. After several cycles, the light source was turned off and potentiostatic EIS measurements were performed at 0.1 V intervals between 0–0.8 V versus  $\text{Fe}(\text{CN})_6^{3-/4-}$  with a frequency range of 3000–200 000 Hz and an AC voltage of 10 rms mV. Between each 0.1 V interval, the system was held at open-circuit until equilibration. The uncompensated series resistance was determined by fitting open-circuit impedance data to an equivalent circuit (see Figure S10 in the Supporting Information).

An FFC solution consisting of  $350 \times 10^{-3} \text{ M}$  potassium hexacyanoferrate(II) trihydrate,  $50 \times 10^{-3} \text{ M}$  potassium



hexacyanoferrate(III), and 1 M KCl was used for light intensity experiments. The solution was magnetically stirred. A graphite reference electrode and Pt wire counter electrode was used. The light intensity was varied from 100 to 40 mW cm<sup>-2</sup>. At each intensity, linear sweep voltammetry was performed with a scan rate of 100 mV s<sup>-1</sup>. The open-circuit photovoltage was measured before and after each linear sweep until stable values were reached.

## Supporting Information

Supporting Information is available from the Wiley Online Library or from the author.

## Acknowledgements

This work was primarily supported by the National Science Foundation (NSF) (CBET-1803991). This work was also supported by the Department of Defense (DoD) through the National Defense Science & Engineering Graduate (NDSEG) Fellowship Program. The synthesis was developed and paid for with the support of the U.S. Department of Energy, Office of Basic Energy Science, Division of Chemical Sciences (FG-02-05ER15686). Secondary support for the development of analytical tools used in the model was provided by NSF (CBET-1702471 and CHE-1800197).

## Conflict of Interest

The authors declare no conflict of interest.

## Keywords

ideality factor, metal–insulator–semiconductor junction, photo-electrochemistry, photovoltage, solar water splitting

Received: October 13, 2019

Revised: January 24, 2020

Published online: February 9, 2020

- [1] M. S. Prévot, K. Sivula, *J. Phys. Chem. C* **2013**, 117, 17879.
- [2] L. C. Seitz, Z. Chen, A. J. Forman, B. A. Pinaud, J. D. Benck, T. F. Jaramillo, *ChemSusChem* **2014**, 7, 1372.
- [3] Y. Chen, S. Hu, C. Xiang, N. S. Lewis, *Energy Environ. Sci.* **2015**, 8, 876.
- [4] T. Wang, J. Gong, *Angew. Chem., Int. Ed.* **2015**, 54, 10718.
- [5] G. Loget, *Curr. Opin. Colloid Interface Sci.* **2019**, 39, 40.
- [6] Z. Luo, T. Wang, J. Gong, *Chem. Soc. Rev.* **2019**, 48, 2158.
- [7] R. Fan, Z. Mi, M. Shen, *Opt. Express* **2019**, 27, A51.
- [8] D. Zhang, J. Shi, W. Zi, P. Wang, S. (Frank) Liu, *ChemSusChem* **2017**, 10, 4324.
- [9] S. Oh, H. Song, J. Oh, *Nano Lett.* **2017**, 17, 5416.
- [10] B. Guo, A. Batool, G. Xie, R. Boddula, L. Tian, S. U. Jan, J. R. Gong, *Nano Lett.* **2018**, 18, 1516.
- [11] S. Oh, J. Oh, *J. Phys. Chem. C* **2016**, 120, 133.
- [12] R. Fan, W. Dong, L. Fang, F. Zheng, M. Shen, *J. Mater. Chem. A* **2017**, 5, 18744.
- [13] B. Seger, L. Pedersen, A. B. Laursen, P. C. K. Vesborg, O. Hansen, I. Chorkendorff, *J. Am. Chem. Soc.* **2013**, 135, 1057.
- [14] F. Song, L. Bai, A. Moysiadou, S. Lee, C. Hu, L. Liardet, X. Hu, *J. Am. Chem. Soc.* **2018**, 140, 7748.
- [15] R. Gao, D. Yan, *Adv. Energy Mater.* **2019**, 9, 1900954.
- [16] D. B. Ingram, S. Linic, *J. Electrochem. Soc.* **2009**, 156, B1457.
- [17] J. Mukherjee, S. Linic, *J. Electrochem. Soc.* **2007**, 154, B919.
- [18] H. Dau, C. Limberg, T. Reier, M. Risch, S. Roggan, P. Strasser, *ChemCatChem* **2010**, 2, 724.
- [19] J. M. Foley, M. J. Price, J. I. Feldblyum, S. Maldonado, *Energy Environ. Sci.* **2012**, 5, 5203.
- [20] P. A. Hernley, S. A. Chavez, J. P. Quinn, S. Linic, *ACS Photonics* **2017**, 4, 979.
- [21] S. Chavez, U. Aslam, S. Linic, *ACS Energy Lett.* **2018**, 3, 1590.
- [22] P. A. Hernley, S. Linic, *J. Phys. Chem. C* **2018**, 122, 24279.
- [23] D. B. Ingram, S. Linic, *J. Am. Chem. Soc.* **2011**, 133, 5202.
- [24] S. Hu, N. S. Lewis, J. W. Ager, J. Yang, J. R. McKone, N. C. Strandwitz, *J. Phys. Chem. C* **2015**, 119, 24201.
- [25] A. G. Scheuermann, P. C. McIntyre, *J. Phys. Chem. Lett.* **2016**, 7, 2867.
- [26] M. F. Lichterman, K. Sun, S. Hu, X. Zhou, M. T. McDowell, M. R. Shaner, M. H. Richter, E. J. Crumlin, A. I. Carim, F. H. Saadi, B. S. Brunschwig, N. S. Lewis, *Catal. Today* **2016**, 262, 11.
- [27] D. Bae, B. Seger, P. C. K. Vesborg, O. Hansen, I. Chorkendorff, *Chem. Soc. Rev.* **2017**, 46, 1933.
- [28] M. Mikolasek, K. Frohlich, K. Husekova, J. Racko, V. Rehacek, F. Chymo, M. Tapajna, L. Harmatha, *Appl. Surf. Sci.* **2018**, 461, 48.
- [29] J. C. Hill, A. T. Landers, J. A. Switzer, *Nat. Mater.* **2015**, 14, 1150.
- [30] O. L. Hendricks, R. Tang-Kong, A. S. Babadi, P. C. McIntyre, C. E. D. Chidsey, *Chem. Mater.* **2019**, 31, 90.
- [31] S. Li, G. She, C. Chen, S. Zhang, L. Mu, X. Guo, W. Shi, *ACS Appl. Mater. Interfaces* **2018**, 10, 8594.
- [32] K. Oh, C. Mériadec, B. Lassalle-Kaiser, V. Dorcet, B. Fabre, S. Ababou-Girard, L. Joanny, F. Gouttefangeas, G. Loget, *Energy Environ. Sci.* **2018**, 11, 2590.
- [33] S. Oh, S. Jung, Y. H. Lee, J. T. Song, T. H. Kim, D. K. Nandi, S.-H. Kim, J. Oh, *ACS Catal.* **2018**, 8, 9755.
- [34] S. A. Lee, T. H. Lee, C. Kim, M. G. Lee, M.-J. Choi, H. Park, S. Choi, J. Oh, H. W. Jang, *ACS Catal.* **2018**, 8, 7261.
- [35] J. Chen, G. Xu, C. Wang, K. Zhu, H. Wang, S. Yan, Z. Yu, Z. Zou, *ChemCatChem* **2018**, 10, 5025.
- [36] C. Li, M. Huang, Y. Zhong, L. Zhang, Y. Xiao, H. Zhu, *Chem. Mater.* **2019**, 31, 171.
- [37] D. V. Esposito, I. Levin, T. P. Moffat, A. A. Talin, *Nat. Mater.* **2013**, 12, 562.
- [38] M. J. Kenney, M. Gong, Y. Li, J. Z. Wu, J. Feng, M. Lanza, H. Dai, *Science* **2013**, 342, 836.
- [39] L. Ji, H.-Y. Hsu, X. Li, K. Huang, Y. Zhang, J. C. Lee, A. J. Bard, E. T. Yu, *Nat. Mater.* **2017**, 16, 127.
- [40] Y. Li, G. Xu, X. Zhu, Z. Man, X. Fu, Z. Hao, Y. Cui, C. Yuan, W. Zhang, S. Yan, H. Ge, Y. Chen, Z. Zou, *Appl. Catal., B* **2019**, 259, 118115.
- [41] G. Loget, C. Mériadec, V. Dorcet, B. Fabre, A. Vacher, S. Fryars, S. Ababou-Girard, *Nat. Commun.* **2019**, 10, 3522.
- [42] A. G. Scheuermann, K. W. Kemp, K. Tang, D. Q. Lu, P. F. Satterthwaite, T. Ito, C. E. D. Chidsey, P. C. McIntyre, *Energy Environ. Sci.* **2016**, 9, 504.
- [43] S. Hu, M. R. Shaner, J. A. Beardslee, M. Lichterman, B. S. Brunschwig, N. S. Lewis, *Science* **2014**, 344, 1005.
- [44] Y. W. Chen, J. D. Prange, S. Dühren, Y. Park, M. Gunji, C. E. D. Chidsey, P. C. McIntyre, *Nat. Mater.* **2011**, 10, 539.
- [45] A. G. Scheuermann, J. P. Lawrence, A. C. Meng, K. Tang, O. L. Hendricks, C. E. D. Chidsey, P. C. McIntyre, *ACS Appl. Mater. Interfaces* **2016**, 8, 14596.
- [46] A. G. Scheuermann, J. P. Lawrence, K. W. Kemp, T. Ito, A. Walsh, C. E. D. Chidsey, P. K. Hurley, P. C. McIntyre, *Nat. Mater.* **2016**, 15, 99.
- [47] M. T. McDowell, M. F. Lichterman, A. I. Carim, R. Liu, S. Hu, B. S. Brunschwig, N. S. Lewis, *ACS Appl. Mater. Interfaces* **2015**, 7, 15189.

- [48] J. Quinn, J. Hemmerling, S. Linic, *ACS Catal.* **2018**, *8*, 8545.
- [49] J. Quinn, J. Hemmerling, S. Linic, *ACS Energy Lett.* **2019**, *4*, 2632.
- [50] M.-J. Park, J.-Y. Jung, S.-M. Shin, J.-W. Song, Y.-H. Nam, D.-H. Kim, J.-H. Lee, *Thin Solid Films* **2016**, *599*, 54.
- [51] I. A. Digdaya, G. W. P. Adhyaksa, B. J. Trzeźniewski, E. C. Garnett, W. A. Smith, *Nat. Commun.* **2017**, *8*, 15968.
- [52] I. A. Digdaya, B. J. Trzeźniewski, G. W. P. Adhyaksa, E. C. Garnett, W. A. Smith, *J. Phys. Chem. C* **2018**, *122*, 5462.
- [53] Z. Luo, B. Liu, H. Li, X. Chang, W. Zhu, T. Wang, J. Gong, *Small Methods* **2019**, *3*, 1900212.
- [54] L. Ji, M. D. McDaniel, S. Wang, A. B. Posadas, X. Li, H. Huang, J. C. Lee, A. A. Demkov, A. J. Bard, J. G. Ekerdt, E. T. Yu, *Nat. Nanotechnol.* **2015**, *10*, 84.
- [55] Q. Cai, W. Hong, C. Jian, J. Li, W. Liu, *ACS Catal.* **2018**, *8*, 9238.
- [56] A. G. Scheuermann, J. D. Prange, M. Gunji, C. E. D. Chidsey, P. C. McIntyre, *Energy Environ. Sci.* **2013**, *6*, 2487.
- [57] Z. Ying, X. Yang, R. Tong, Q. Zhu, T. Chen, Z. He, H. Pan, *ACS Appl. Energy Mater.* **2019**, *2*, 6883.
- [58] M. Ritala, M. Leskelä, *Nanotechnology* **1999**, *10*, 19.
- [59] H. C. Card, E. H. Rhoderick, *J. Phys. D: Appl. Phys.* **1971**, *4*, 1589.
- [60] L. F. Wagner, R. W. Young, A. Sugerman, *IEEE Electron Device Lett.* **1983**, *4*, 320.
- [61] E. H. Rhoderick, *IEE Proc., Part I: Solid-State Electron Devices* **1982**, *129*, 1.
- [62] Ş. Altındal, S. Karadeniz, N. Tuğluoğlu, A. Tataroğlu, *Solid-State Electron.* **2003**, *47*, 1847.
- [63] I. Ohdomari, K. N. Tu, F. M. d'Heurle, T. S. Kuan, S. Petersson, *Appl. Phys. Lett.* **1978**, *33*, 1028.